WILEY

RESEARCH ARTICLE

A wind field downscaling strategy based on domain segmentation and transfer functions

Jordi Barcons[1,2] | Matias Avila[1] | Arnau Folch[1]

[1]Barcelona Supercomputing Center, Barcelona 08034, Spain

[2]Meteorological Service of Catalonia, Barcelona, 08029, Spain

Correspondence

Jordi Barcons, Barcelona Supercomputing Center, Nexus II Building, Jordi Girona, 29, Barcelona 08034, Spain.
Email: jordi.barcons@bsc.es

Abstract

This paper presents a novel methodology for mesoscale-to-microscale downscaling of near-surface wind fields. The model chain consists on the Weather Research and Forecast mesoscale model and the Alya-CFDWind microscale model (assuming neutral stability). The downscaling methodology combines precomputed microscale simulations with a mesoscale forecast using a domain segmentation technique and transfer functions. As a result, the downscaled wind field preserves the mesoscale pattern but, at the same time, incorporates local mesoscale subgrid terrain effects, particularly at valleys and channelling zones. The methodology has been validated over a 9-month period on a very complex terrain site instrumented with a dense observational network of meteorological masts. With respect to mesoscale results, the global skills of the downscaled wind at masts improve for wind direction and remain similar for wind velocity. However, a substantial improvement occurs under stable and neutral conditions and for high wind velocity regimes.

KEYWORDS

complex terrain, downscaling, high-resolution, near-surface winds, transfer functions, wind forecast

1 | INTRODUCTION

Near-surface wind fields are typically obtained from mesoscale Numerical Weather Prediction (NWP) models that describe the physics and dynamics of the atmosphere in the mesoscale range, ie, covering phenomena with characteristic dimensions spanning from several hundreds down to few kilometres (at the edge of the meso-γ scale, eg, Orlanski[1]). Operational configurations of mesoscale NWP models use horizontal grid resolutions from tens to ~ 1 km. These terrain discretizations are often insufficient to capture flow effects over complex terrains, where the near-surface winds are strongly influenced by mesoscale subgrid topographic features. However, high-resolution (tens to hundreds of metres) near-surface wind fields can be important in applications where microscale topographic features and terrain roughness exert a major control on the wind flow. Some of these applications include wind resource evaluation, wind power forecast, or simulation of wind-driven hazardous phenomena such as wildfire spreading or atmospheric dispersion of pollutants and toxic substances. In these cases, some mesoscale-to-microscale downscaling strategy turns necessary.

Traditionally, high-resolution near-surface microscale winds have been obtained by means of mass-consistent diagnostic models (eg, Kitada et al and Homicz[2,3]). These models enforce the conservation of mass and, in some cases, include also additional parameterisations to approximate (not solve) microscale effects such as wind channelling and thermal slope flows. In this case, the downscaling strategy consists on obtaining an initial guess wind field from a mesoscale NWP model, which is then projected over the finer complex terrain grid applying some divergence minimisation procedure (eg, Wagenbrenner et al[4]). This methodology works well in simple cases but fails in representing phenomena such as recirculation behind obstacles, vortex shedding, or surface boundary layer profiles (eg, Ehrhard et al[5]), for which a more complex approach is needed. On the other hand, the increase in computational power is extending rapidly the use of Computational Fluid Dynamics (CFD) models for atmospheric simulations

(eg, Arroyo et al, Castro et al, and Udina et al[6-8]), including both steady or unsteady Reynolds-Averaged Navier-Stokes (RANS/URANS) and Large Eddy Simulation (LES) models; all with turbulence closures and wall laws adapted to atmospheric flows. The CFD-based models explicitly solve the momentum (and eventually energy) equations and, therefore, can capture physical phenomena that are not implicit in the simpler mass-consistent models. However, open issues still exist regarding the optimal strategies for dynamic NWP-to-CFD (meso-to-micro) model coupling (eg, Castro et al and Zajaczkowski et al[7,9]), including inconsistencies between the physics of models across scales or the imposition of suitable boundary conditions for nesting.[5,10] Different downscaling strategies are being a subject of active research within the wind engineering community, but in meteorology and numerical weather prediction, progress is running more slowly. One of the reasons for this is that the computational cost of CFD models still precludes the use of dynamical downscaling strategies in routine simulations and in operational weather forecast environments.

This paper presents an alternative cost-efficient wind field downscaling strategy that introduces microscale information from precomputed CFD simulations into a mesoscale solution/forecast. The downscaling methodology combines a domain segmentation technique with transfer functions, a concept originally proposed for microscale wind resource assessment over regional scales.[11] Here, we extend the concept of transfer functions to forecast near-surface high-resolution winds by combining a mesoscale forecast with a set of microscale precomputed CFD reference simulations. This adds little extra cost to the operational model chain and supposes a compromise between simpler mass-consistent downscaling and dynamic NWP-to-CFD coupling, too costly in terms of operational forecast. Section 2 describes the 2 models adopted for the model chain, the Weather Research Forecast (WRF) model for the mesoscale and the Alya-CFDWind model for the microscale. Section 3 introduces the downscaling methodology based on domain segmentation and transfer functions. A case study for validation is presented in Section 4 for a site in the Mexican state of Puebla, characterised by a very complex orography. This site has been instrumented with eleven 80-m height meteorological masts by a wind energy company with a prospective scope. Section 5 shows the validation results for a 9-month period, used to quantify the gain in the downscaled wind field with respect to the mesoscale WRF forecast depending on wind intensity and atmospheric stability. Finally, Section 6 contains a summary and a discussion on the limitations of the methodology and on its future improvements.

2 | MODEL CHAIN COMPONENTS

2.1 | WRF-ARW mesoscale model

The WRF is a mesoscale NWP model and atmospheric simulation system designed to serve both operational forecasting and atmospheric research needs.[12] It is a fully compressible, non-hydrostatic model using finite differences schemes on a staggered horizontal Arakawa C-grid and a terrain-following vertical coordinate system. Here, we use the version 3.4.1 of the dynamical solver Advanced Research WRF (WRF-ARW), configured with the physical parameterisations and schemes listed in Table 1.

2.2 | Alya-CFDWind microscale model

Alya-CFDWind[20] is a CFD model for the Atmospheric Boundary Layer (ABL) based on the Reynolds-Averaged Navier-Stokes (RANS) equations and a $\kappa - \epsilon$ turbulence model adapted to atmospheric flows in complex terrains. The model considers Coriolis effects, a consistent limitation of the mixing length,[21] and a wall law for atmospheric boundary layers (logarithmic profile depending on terrain roughness and wind friction velocity). Alya-CFDWind is implemented as a module in Alya, a High Performance Computing (HPC) multiphysics parallel solver based on Finite Element Methods (FEM)[22,23] and is routinely used in the context of wind energy to solve atmospheric flows in complex terrains. A set of preprocess software tools[24] is used to assimilate terrain information and generate structured meshes made of hexahedral elements. The computational domains consist of an external flat buffer (used to accommodate the entering flow), an adjacent transition zone, and an inner higher-resolution zone having the real topography (region of interest). The same preprocess tools generate inflow boundary conditions consistent with the atmospheric boundary layer by means of a 1D precursor.

2.2.1 | Governing equations of Alya-CFDWind microscale model

The Alya-CFDWind governing equations are the incompressible RANS Equations 1 and 2, together with a $k - \epsilon$ turbulence models (3) and (4). The model accounts for Coriolis force due to Earth rotation and uses a consistent limitation of the mixing length.[21] The resulting system of equations is

$$\text{Mass equation} \qquad \nabla \cdot \mathbf{u} = 0, \tag{1}$$

$$\text{Momentum equation} \qquad \frac{\partial \mathbf{u}}{\partial t} + \mathbf{u} \cdot \nabla \mathbf{u} - \nabla \cdot \left(\nu_t \nabla^s \mathbf{u} \right) = -\boldsymbol{\nabla} p - 2\boldsymbol{\omega} \times \mathbf{u}, \tag{2}$$

$$\text{TKE equation} \qquad \frac{\partial k}{\partial t} + \mathbf{u} \cdot \nabla k - \nabla \cdot \left(\frac{\nu_t}{\sigma_k} \nabla k \right) = P_k - \epsilon, \tag{3}$$

$$\text{TKE dissipation equation} \qquad \frac{\partial \epsilon}{\partial t} + \mathbf{u} \cdot \nabla \epsilon - \nabla \cdot \left(\frac{\nu_t}{\sigma_\epsilon} \nabla \epsilon \right) = \frac{\epsilon}{k} \left(C_1' P_k - C_2 \epsilon \right), \tag{4}$$

TABLE 1 Physical parameterisations for the WRF-ARW model (version 3.4.1) configuration

WRF-ARW 3.4.1 Physical Schemes	
Microphysics	WRF single-moment 6-class (WSM6)[13]
Cumulus	Modified Kain-Fritsch[14]
Surface Layer	ETA Monin-Obukhov[15]
Land Surface	Unified Noah Land Surface Model (LSM)[16]
Planet Boundary Layer	Mellor Yamada Janjic (MYJ)[17]
Long-wave Radiation	Rapid Radiative Transfer Model (RRTM)[18]
Short-wave Radiation	Dudhia[19]

TABLE 2 Alya-CFDWind model coefficients

κ	C_μ	C_1	C_2	σ_k	σ_ϵ
0.4	0.033	1.176	1.92	1.0	1.238

where the unknowns are the wind velocity vector $\mathbf{u}$, the pressure p, the turbulent kinetic energy (TKE) k and its dissipation rate ϵ. The turbulent viscosity ν_t is given by

$$\nu_t = \frac{C_\mu k^2}{\epsilon}.$$ (5)

In the momentum equation, ∇^s refers to the symmetric gradient operator. The second term in the right-hand side of Equation 2 is the Coriolis force term, being $\boldsymbol{\omega}$ the Earth's angular velocity. In Equations 3 and 4, P_k is the TKE production rate by mechanical shear. The coefficient C_1' in the right-hand side of Equation 4 is a modified coefficient, originally proposed by Apsley and Castro,[21] that limits the mixing length below a maximum l_{max} for neutral flows, computed as[25]

$$l_{max} = 0.00027 \frac{|\mathbf{u_g}|}{2|\boldsymbol{\omega}|\sin\lambda},$$ (6)

where λ is the latitude and $\mathbf{u_g}$ is the geostrophic wind velocity. Finally, Table 2 shows the used Alya-CFDWind coefficients.

2.2.2 | Boundary conditions

The boundaries of the computational domain are classified as bottom, top, lateral inflow, and lateral outflow.

- **On the bottom boundary**, wall law functions following the Monin-Obukhov similarity theory[26] are imposed for momentum and turbulence equations to remove a boundary layer of thickness δ_w above z_0. Thus, the shear stress τ_{wall} is imposed in terms of the wind velocity component parallel to the ground $\mathbf{u}_{tan}$ at distance δ_w above the ground, as

$$|\mathbf{u}_{tan}(\delta_w)| = \frac{u_*}{\kappa} \ln\left(1 + \frac{\delta_w}{z_0}\right),$$ (7)

where u_* is the friction velocity $u_* = (\tau_{wall}/\rho)^{1/2}$ and z_0 is the terrain roughness length. A zero diffusion through the wall is imposed for the turbulent kinetic energy ($\nabla k \cdot \mathbf{n} = 0$, with $\mathbf{n}$ the normal vector to the wall) and the dissipation rate is imposed as

$$\epsilon(\delta_w) = \frac{k^{3/2} C_\mu^{3/4}}{\kappa (\delta_w + z_0)}.$$ (8)

- **On the top boundary**, symmetry boundary conditions (zero normal gradient to the wall) are imposed for the tangential velocity component, θ, k, and ϵ. The normal velocity component is fixed to zero (ie, $\mathbf{u} \cdot \mathbf{n} = 0$).
- **On the lateral inflow boundary**, vertical profiles for $\mathbf{u}$, θ, k, and ϵ are imposed from a 1D precursor simulation assuming uniform roughness and flat terrain.
- **On the lateral outflow boundaries**, symmetry boundary conditions are imposed for θ, k, and ϵ. For the momentum equation, the geostrophic pressure and no shear stress are imposed.

3 | DOWNSCALING METHODOLOGY

We propose a downscaling methodology that links the different components of the model chain using a combination of domain segmentation and transfer functions.[11] This methodology constructs a downscaled wind from a WRF wind field (forecast) and a set of precomputed steady-state
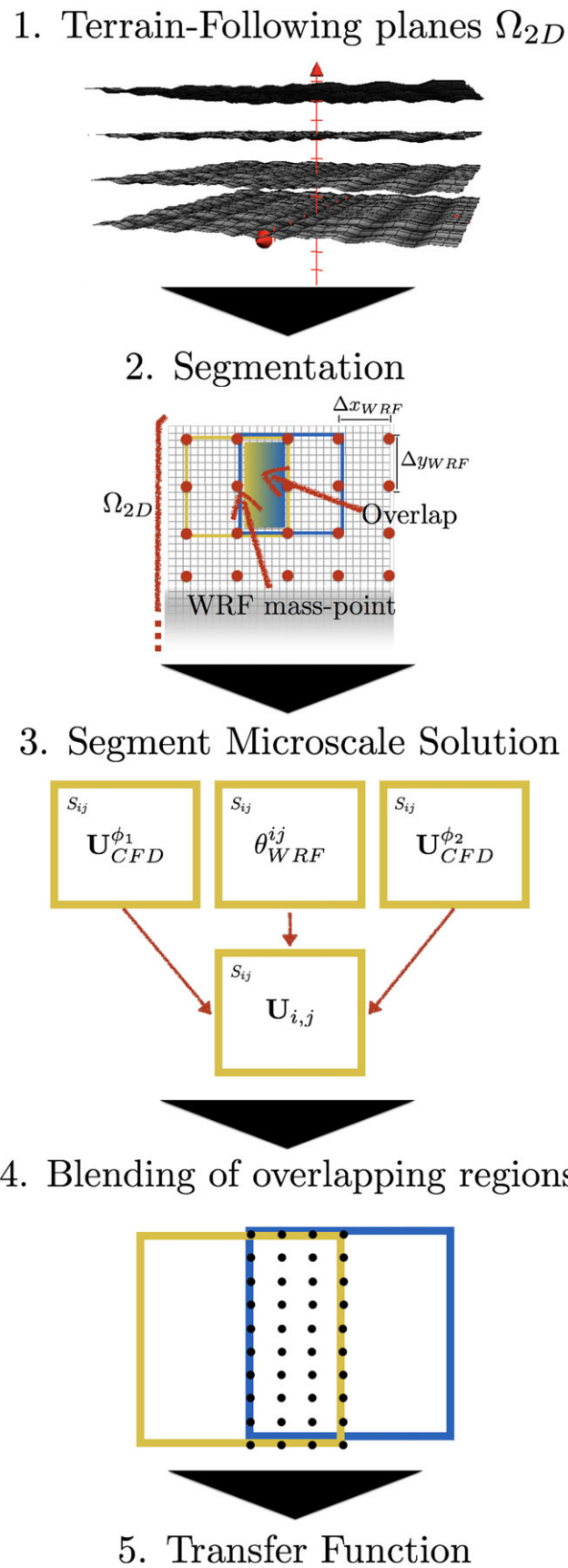
1. Terrain-Following planes Ω_{2D}

2. Segmentation

Δx_{WRF}

Δy_{WRF}

Ω_{2D}

Overlap

WRF mass-point

3. Segment Microscale Solution

S_{ij} $\mathbf{U}_{CFD}^{\phi_1}$

S_{ij} θ_{WRF}^{ij}

S_{ij} $\mathbf{U}_{CFD}^{\phi_2}$

S_{ij} $\mathbf{U}_{i,j}$

4. Blending of overlapping regions

5. Transfer Function

FIGURE 1 Steps of the downscaling methodology giving the wind field on a series of terrain-following Ω_{2D} planes using domain segmentation and transfer functions [Colour figure can be viewed at wileyonlinelibrary.com]

microscale reference solutions from the Alya-CFDWind solver. The resulting downscaled wind field keeps the mesoscale pattern but, at the same time, incorporates the microscale fluctuations at a local scale. This methodology is very attractive from the point of view of operational forecasting because the downscaling is performed for the area(s) of interest at the post-process stage. Thus, as opposed to a pure CFD dynamical downscaling or to a simpler mass-consistent approach, our methodology supposes no extra computational cost during operations.

The starting point of the downscaling is a WRF simulation (forecast) plus a set of precomputed Alya-CFDWind runs covering the downscaling target area(s). Each of these Alya-CFDWind reference simulations ($\mathbf{U}_{CFD}^{\varphi}$) is computed a priori imposing a geostrophic wind direction φ prescribed at the top of the computational domain. The 360° possible geostrophic wind directions are discretised assuming bins of constant width, eg, a set of 16 precomputed simulations results on a 22.5° geostrophic (top) wind binning. However, note that because of Coriolis and terrain effects, winds from Alya-CFDWind twist with height, resulting on nonequally spaced bin direction increments as height decreases from top to surface. The downscaling methodology involves a series of steps (Figure 1):

1. The first step consists on constructing a series of 2D terrain-following grids Ω_{2D} at user-defined elevations above the terrain (eg, $z_t = 10, 20,$ and 50 m) where the downscaled wind will actually be computed. Both the mesoscale (WRF) and the microscale (precomputed Alya-CFDWind) wind fields need to be interpolated to the nodes of these Ω_{2D} grids.

2. Each of these Ω_{2D} planes is then decomposed on a series of structured segments S_{ij} centered at the position of the WRF grid mass point. The area of the segments is $2\Delta x_{WRF} \times 2\Delta y_{WRF}$, where Δx_{WRF} and Δy_{WRF} are the WRF cell dimensions. This defines regions of overlap between segments (ie, $\cup S_{ij} = \Omega_{2D}$ and $\cap S_{ij} \neq \varnothing$) to allow obtaining a smooth solution in the domain reconstruction step. The purpose of this domain segmentation is to have a reference mesoscale wind direction θ_{WRF}^{ij} (that corresponds to the WRF grid mass-point wind direction) for each segment S_{ij}.

3. For each segment S_{ij} and time t, the direction θ_{WRF}^{ij} is used to build a segment microscale solution ($\mathbf{U}_{ij}$) by performing a linear interpolation between the 2 precomputed runs $\mathbf{U}_{CFD}^{\varphi_1}$ and $\mathbf{U}_{CFD}^{\varphi_2}$ that bound θ_{WRF}^{ij} (ie, $\theta_{WRF}^{ij} \in (\varphi_1, \varphi_2)$). In this way, and by construction, the average of the microscale wind direction of $\mathbf{U}_{ij}$ coincides with that of the mesoscale θ_{WRF}^{ij}.

4. Small variations of θ_{WRF}^{ij} can occur across adjacent segments S_{ij}, resulting on small differences on wind velocity and direction at nodes in the overlapping regions. To have a smooth transition between these adjacent $\mathbf{U}_{ij}$ solutions, a smoothing operation is performed at the overlap regions between segments. In particular, we consider a linear weighted interpolation for each horizontal wind component. The blending of all segment microscale solutions $\mathbf{U}_{ij}$, on both latitudinal and longitudinal directions, results on an intermediate microscale field $\mathbf{U}_{inter}$.

5. Finally, the transfer functions are applied to scale the modulus of the microscale wind at each point of the Ω_{2D} planes as

$$|\mathbf{U}_{down}| = f|\mathbf{U}_{WRF}| = \frac{|\mathbf{U}_{inter}|}{<|\mathbf{U}_{inter}|>_{\Re}}|\mathbf{U}_{WRF}|, \tag{9}$$

where $\mathbf{U}_{down}$ is the resulting downscaled wind velocity, $f(x, y, z, t)$ is the point-dependent transfer function at time t, $\mathbf{U}_{WRF}$ is the WRF wind velocity modulus interpolated at the point, $\mathbf{U}_{inter}$ is the microscale wind velocity resulting from step 4, and $<\mathbf{U}_{inter}>_{\Re}$ is the spatial average of $\mathbf{U}_{inter}$ over a radius of influence $\Re$. Note that, by construction, when $\Re \to 0$, the downscaled wind velocity tends to that of WRF ($\mathbf{U}_{down} \to \mathbf{U}_{WRF}$). In contrast, as $\Re$ increases, the transfer functions incorporate to the downscaled field the local wind fluctuations caused by microscale topographic forcing.

Some critical aspects of the methodology have to be mentioned. First, the horizontal resolution of the mesoscale model should be sufficiently coarse to avoid, as much as possible, a double counting of terrain forcing effects. It means that the WRF model should not account for the microscale flow characteristics that are explicitly resolved by the Alya-CFDWind solver. Second, the domain segmentation technique is designed to guarantee that the downscaled field preserves locally the WRF wind direction on average (the mesoscale pattern). Third, the transfer functions are used to scale (correct) the WRF wind velocity accounting for terrain speed-up and slow-down effects.

4 | VALIDATION TEST CASE

4.1 | Site description

The validation considers a site in the Mexican state of Puebla characterised by a very complex orography. The area is located at about 20 km south of Pico de Orizaba volcano (5636 m asl, the highest Mexican peak) and near the town of Esperanza, on a plateau with an averaged elevation of 2400 m. The predominant yearly wind direction is westward, where east winds coming from the Gulf of Mexico pass first over a vast flat area and then, when approaching the region of interest, encounter a complex orography with high mountain slopes and channelling zones on the way up to the plateau.

This site was selected for validation because of access to a long-period dataset acquired by a private company during a wind resource prospection campaign. Wind data comes from a very dense network of 11 met masts (Figure 2) instrumented with sonic anemometers at 40, 60, and 80 m height, with a total period of acquisition of 3 years (not synchronous in all masts). The acquisition frequency of sensors is of 1 Hz, with instantaneous values averaged over 10-minute periods. For validation, we used the 9-month period from June 2013 to February 2014, for which a continuous and synchronous record exists for all masts. The advantage is that to dispose of a dataset of such a spatial density over a long-period of time is unusual. However, the drawback is that met masts were deployed at elevated zones, away from deep valley bottoms and channelling zones. This can
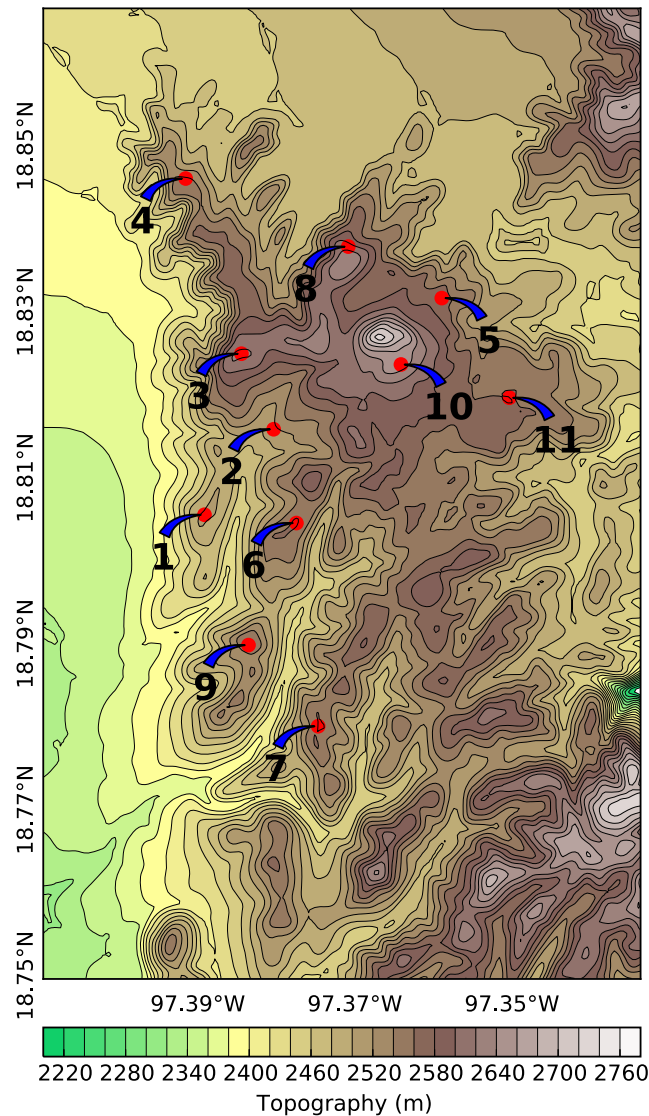
FIGURE 2 Elevation contours (in metre asl) of the area of interest and location of the 11 met masts deployed for wind resource assessment. The area shown is 8×13 km^2 [Colour figure can be viewed at wileyonlinelibrary.com]

constrain our model validation because no large differences are expected between mesoscale and downscaled microscale winds at mast locations. Note that a similar problem would occur with surface Automatic Weather Stations (AWS) because, typically, AWS are also deployed at locations where the mesoscale component of the wind dominates. This private dataset is confidential and, for this reason, we can not show period (yearly) absolute values of wind speed throughout this paper. Wind values will be given normalised to the mean observed winds, with no absolute error differences shown.
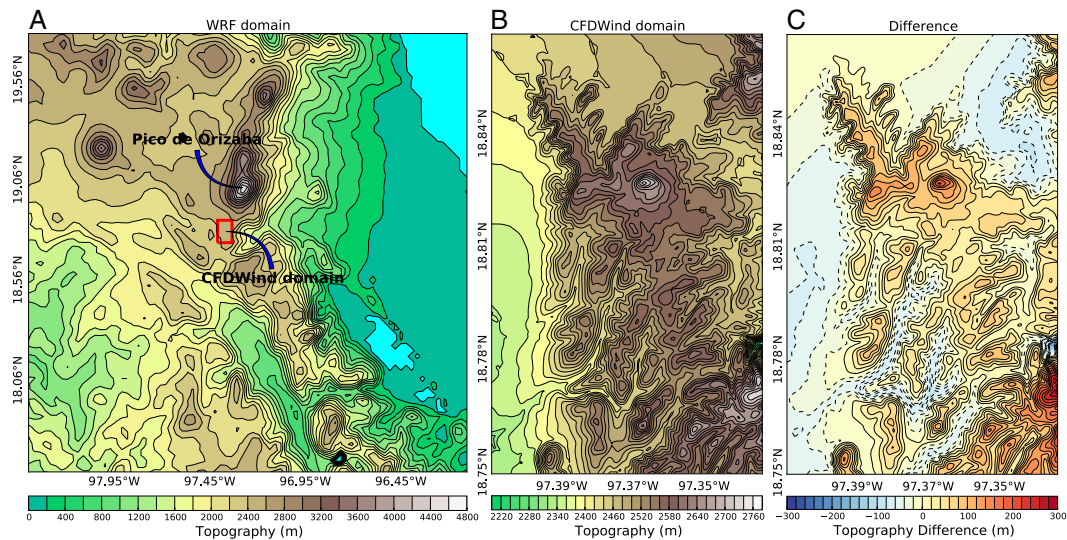
4.2 | WRF-ARW model setup

The WRF model was configured as summarised in Table 3 with the physical parameterisations listed in Table 1. The simulated period (9 months) is covered by overlapping 48-hour model runs, allowing 24 hours for model spin-up and with a model output period of 30 minutes. Initial and 3-hourly boundary conditions for each run come from the European Centre for Medium-Range Weather Forecasts (ECMWF) operational deterministic model at 0.125° resolution.[27] Figure 3A shows the WRF computational domain and the topography contours at 3-km model resolution. The domain is centred near the Pico de Orizaba volcano, covering an area of 255×255 km^2.

4.3 | Alya-CFDWind model setup

The Alya-CFDWind computational domain (Figure 4) consists of an inner region of 8×13 km^2 at 40-m horizontal grid resolution surrounded by a transition zone in which the size of the elements increases up to that of the external buffer zone, having no topography and used to accommodate the

TABLE 3 Configuration of the WRF-ARW model for the Puebla test case

WRF-ARW Configuration	
Model version	3.4.1
Initial and lateral BCs	ECMWF at 0.125° resolution
Domains	1
Horizontal grid resolution	3 km
Horizontal grid size	86 × 86
Vertical levels	60 levels, with top at 50 hPa
Simulation length	48 h (spin-up of 24 h)
Integration time step	20 s

FIGURE 3 A, WRF computational domain and topography contours (255×255 km^2). B, Downscaling area showing the Alya-CFDWind topography contours (8×13 km^2). The red box in the WRF domain shows the location of the Alya-CFDWind computational domain. C, Topography differences between WRF (at 3-km resolution) and Alya-CFDWind (40-m resolution) [Colour figure can be viewed at wileyonlinelibrary.com]

incoming flow. The height of the buffer zone corresponds to the minimum height of the contour of the transition zone. Along the vertical direction, the structured grid extends up to 5.5 km above the ground, with 56 vertical layers growing geometrically in size from 1 m at surface to 250 m at top. The resulting computational mesh has around 12.5M grid points. The Coriolis force corresponds to that of a latitude 18.8° N, and the maximum mixing length is calculated automatically by the model depending on the wind velocity at top and the Coriolis force as in Apsley and Castro.[21] The pressure gradient $\nabla p = 2\boldsymbol{\omega} \times \mathbf{u}_g$ is fixed over the whole domain, where $|\mathbf{u}_g| = 17.5$ m s^{-1} is the geostrophic wind vector, ρ is the air density, and ω is the Earth's angular velocity vector. With these conditions, we performed one Alya-CFDWind simulation for each reference direction (sector) of the geostrophic wind using 22.5° binning (ie, 16 different runs were needed to scan all geostrophic directions). Assuming self-similarity, these precomputed reference runs are then scaled and interpolated during the downscaling process depending on the WRF model outputs.

A convergence mesh study has been done for the present case running 3 simulations. Simulation **A** uses a mesh of 40 m horizontal resolution in the farm zone, 1 m of first element vertical length, and 56 vertical levels. Simulation **B** uses the mesh of simulation **A** with each element divided in 8 new elements, halving the length of each element edge. This mesh has the same topography as simulation **A**. Simulation **C** uses a mesh with the same number of elements of simulation **B** but assimilating the topography with higher resolution. Table 4 presented the percentage (%) of the wind velocity difference between the 3 different simulations of the 90.0° sector. The goal is to quantify how much the obtained solution is modified when the mesh is refined horizontally and vertically (column **A** vs **B** in Table 4), and when also a more detailed topography is assimilated because of the higher mesh resolution (columns **A** vs **C** and **B** vs **C** in Table 4). The absolute differences are computed at 11 masts (see Figure 2) at 80-m height above terrain. Results show that the mesh refinement halving the mesh element length (8 times more elements) (from 40-m horizontal grid resolution to 20 m, and from 56 vertical levels to 112) the solution at masts changes a 4.2 % on average. In addition, if the higher resolution entails the assimilation of a more detailed topography, the solution changes a 4.7 % on average. Finally, if we only evaluate the effect of assimilating, a more detailed topography using the finer mesh, the solution changes a 4.6 % on average. Figure 5 shows the wind velocity module vertical profiles at 4 of the 11 masts evaluated. It is observed that the profiles at Mast 7 and Mast 11 locations are much more modified when assimilating more terrain than
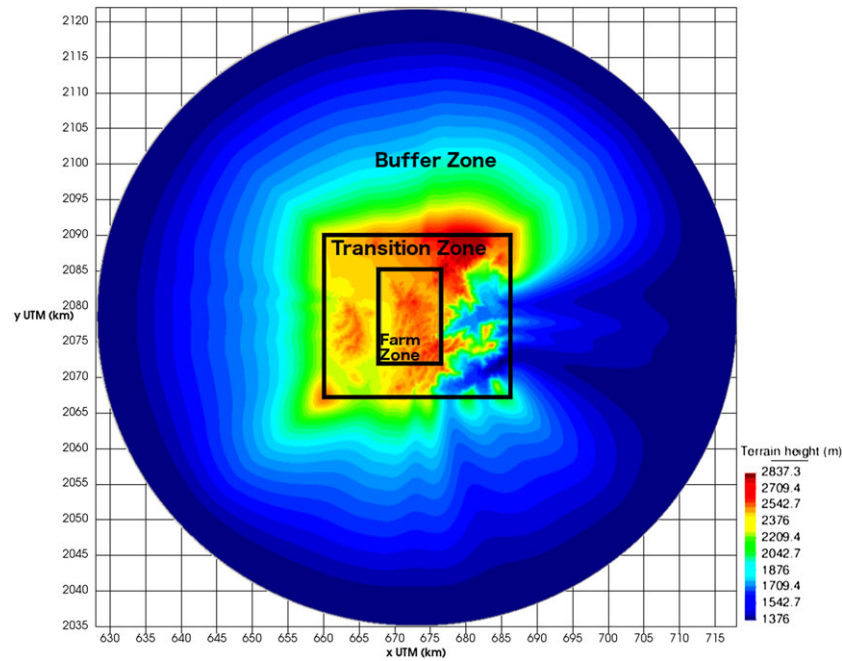
FIGURE 4 Alya-CFDWind computational domain with 3 different mesh zones identified: a 8 × 13 km² farm zone with 40-m horizontal grid resolution (ie, the downscaling area, see Figure 3B), a transition zone extending 5 km to the North and South, 8 km to the West, and 10 km to the East respectively, and an external flat buffer zone [Colour figure can be viewed at wileyonlinelibrary.com]

TABLE 4 Percentage (%)wind velocity module difference at 11 masts at 80-m height (see Figure 2) between 3 different simulations of the 90.0° sector

Mast	A vs B	A vs C	B vs C
1	2.9	2.9	6.0
2	0.1	1.8	1.8
3	9.6	6.8	2.6
4	1.5	11.1	10.8
5	13.2	3.6	9.3
6	3.3	1.0	2.3
7	1.1	6.5	8.2
8	1.0	4.0	3.1
9	8.3	6.1	2.3
10	4.5	5.4	0.9
11	0.8	2.5	3.4
Ave	4.2	4.7	4.6

Note: **A** simulation used a mesh at 40-m horizontal grid resolution with 56 vertical levels. **B** simulation used a mesh at 20-m horizontal grid resolution, 112 vertical levels but without assimilating new topography regarding **A**. **C** used a mesh at 20-m horizontal grid resolution, 112 vertical levels and assimilating new topography regarding **A** thanks to the higher resolution.

when simply refining the mesh resolutions. However, Mast 3 and Mast 9 show an important modification of the solution due to the mesh refinement and not due to the better terrain assimilation.

4.4 | Downscaling setup

The downscaling methodology described in Section 3 was applied every 30 minutes for each WRF model output at near-surface terrain-following levels of 10, 20, 40, 60, and 80 m (ie, using 5 different Ω_{2D} planes for downscaling). To assess the optimal radius of influence $\Re$ for the transfer
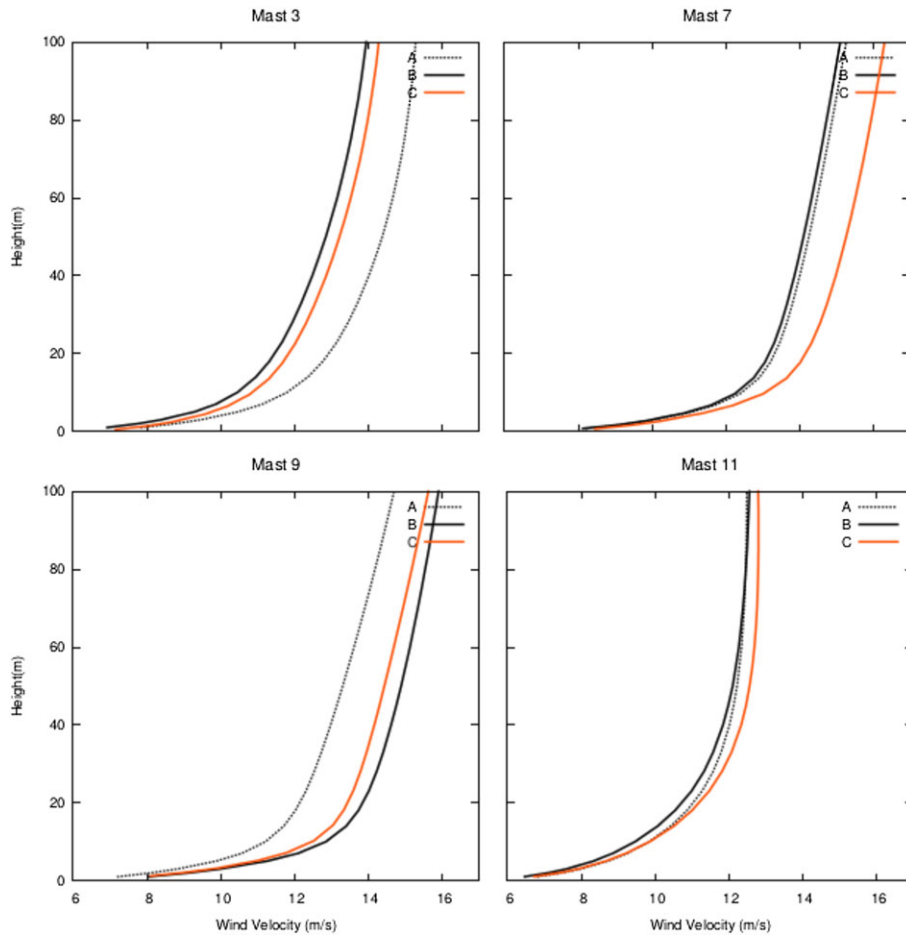
FIGURE 5 Wind velocity module vertical profiles of 4 masts (see Figure 2) comparing 3 different simulations of the 90.0° sector: **A** simulation used a mesh at 40-m horizontal grid resolution with 56 vertical levels. **B** simulation used a mesh at 20-m horizontal grid resolution, 112 vertical levels but without assimilating new topography regarding **A**. **C** used a mesh at 20 m horizontal grid resolution, 112 vertical levels and assimilating new topography regarding **A**, thanks to the higher resolution [Colour figure can be viewed at wileyonlinelibrary.com]

functions (see Equation 9), the downscaling methodology was considered under 4 different cases of $\Re = 150$ m ($\Re_{150}$), $\Re = 250$ m ($\Re_{250}$), $\Re = 500$ m ($\Re_{500}$), and $\Re = 1000$ m ($\Re_{1000}$). As previously mentioned, this radius affects the weight given to the mesoscale and the microscale contributions on the resulting downscaled solution respectively.

4.5 | Validation metrics

The following metrics were used to validate quantitatively the downscaling methodology for all masts over the 9-month period:

1. Mean Error (ME) for wind velocity:

$$\text{ME}(f, o) = \frac{1}{n} \sum_{i=1}^{n} (f_i - o_i)$$

equivalent to the bias, the ME gives information of wether wind speed forecasts (f_i) are, on average, overestimating (positive values) or underestimating (negative values) observations (o_i).

2. Root Mean Square Error (RMSE) for wind velocity and direction:

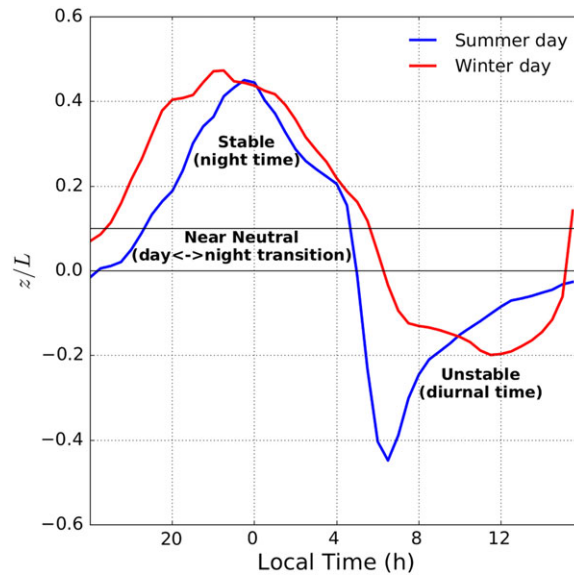$$\text{RMSE}(f, o) = \sqrt{\frac{1}{n} \sum_{i=1}^{n} (f_i - o_i)^2}$$

FIGURE 6 Values of z/L during a summer and a winter cloud-free diurnal cycle. The specific days are August 8, 2013 and January 5, 2014, respectively. The different stability regimes are shown [Colour figure can be viewed at wileyonlinelibrary.com]

gives additional information about the deviation of forecasts from observations.

3. Skill Score (SS%) for wind velocity and direction:

$$\text{SS\%}(f, r, o) = 100 \left(1 - \frac{\text{MSE}(f, o)}{\text{MSE}(r, o)} \right),$$

where MSE is the Mean Square Error. The SS% can be interpreted as the accuracy of the model under evaluation (f) relative to a reference model (r). This index penalises large differences between forecasts and observations (o).

4.6 | Classification of atmospheric stability

The mesoscale WRF wind fields implicitly include atmospheric stability information. In contrast, the precomputed microscale Alya-CFDWind fields assume neutral stability but account for local-scale terrain effects. For this reason, differences in the downscaling skill scores could exist under different atmospheric stability conditions and wind intensities. To desegregate these effects, we distinguishing 3 different stability classes as

$$\begin{cases} z/L > 0.1 & \text{stable} \\ 0.1 \geq z/L \geq 0 & \text{near neutral} \\ z/L < 0 & \text{unstable} \end{cases},$$

where z is the height of the layer used to calculate L, the Obukhov length from the Monin-Obukhov similarity theory[26]:

$$L = \frac{\rho c_p}{\kappa \alpha} \frac{u_*^3}{\mathbf{g} \cdot \mathbf{q}},$$

where c_p is the air heat capacity, ρ is the air density, u_* is the friction velocity, κ is the von Kármán constant, α is the thermal expansion coefficient, $\mathbf{g}$ is the gravity vector, and $\mathbf{q}$ is the surface heat flux vector. Figure 6 shows the dimensionless stability parameter z/L during 2 cloud-free 24-hour periods. Note that z/L changes its sign (from positive to negative) around sunrise, when buoyancy forces foster air mixing and the atmospheric boundary layer grows in height. This period, which ends after noon, is typically dominated by convection. In contrast, z/L becomes positive during the evening, where convective forces near surface almost vanish and the atmosphere passes through a short period of near neutral stability.

5 | RESULTS

5.1 | Qualitative evaluation

Before performing a full-period quantitative validation, it is illustrative to show the downscaling results for a particular 24-hour period characterised by a persistent easterly situation, the predominant wind direction over the region. In the methodology, the resulting downscaled wind direction comes exclusively from the domain segmentation and overlapping processes. The RMSEs values (all measuring heights computed together) for this

particular day are 10.4° for the downscaled field in front of 11.1° for WRF. On the other hand, the near-surface wind velocity fields after applying the transfer functions depend on the value of $\Re$. Table 5 lists the values of RMSE and SS% obtained for different values of $\Re$. As observed, for this particular day, the lower RMSE and the best skill score are obtained with a radius of influence of $\Re_{500}$. This value will be assumed throughout this section.

Figure 7 compares the 10-m wind velocity fields from the precomputed Alya-CFDWind model, the WRF model and the downscaling methodology. This figure highlights the local terrain information contained in the precomputed microscale solution (Figure 7A) in front of the smoother field provided by the much coarser WRF model at 3-km resolution (Figure 7B). Clearly, the resulting downscaled field (Figure 7C) contains the general mesoscale pattern but modulated by the local-scale terrain information added by the CFD model. Figure 8 compares the mesoscale and the downscaled wind fields at the same time instant over a small region of about 3×3 km^2 (one WRF cell size) that includes Mast-7. Note how the downscaled field speeds up the wind flow at the top of the ridges while, in contrast, winds slow down and rotate at valleys and channelling zones. For this particular time instant, the differences in wind direction and velocity between WRF and the downscaled field at the valley (red dot in Figure 8) are of 77.8° and 3.3 m s^{-1}, respectively. These differences are mainly due to the terrain channelling effects. Figure 9 shows the differences between the downscaled and the WRF mesoscale wind velocities depending on the value of $\Re$. As observed, the smaller the value of $\Re$, the more the downscaled

TABLE 5 Values of RMSE (in m s^{-1}) and Skill Score (SS%) for the 24-h period selected using 30-minute data from the 11 met masts

	RMSE	SS%
WRF	2.6	0.0
$\Re_{150}$	2.6	0.9
$\Re_{250}$	2.5	4.1
$\Re_{500}$	2.4	6.0
$\Re_{1000}$	3.1	−18.3

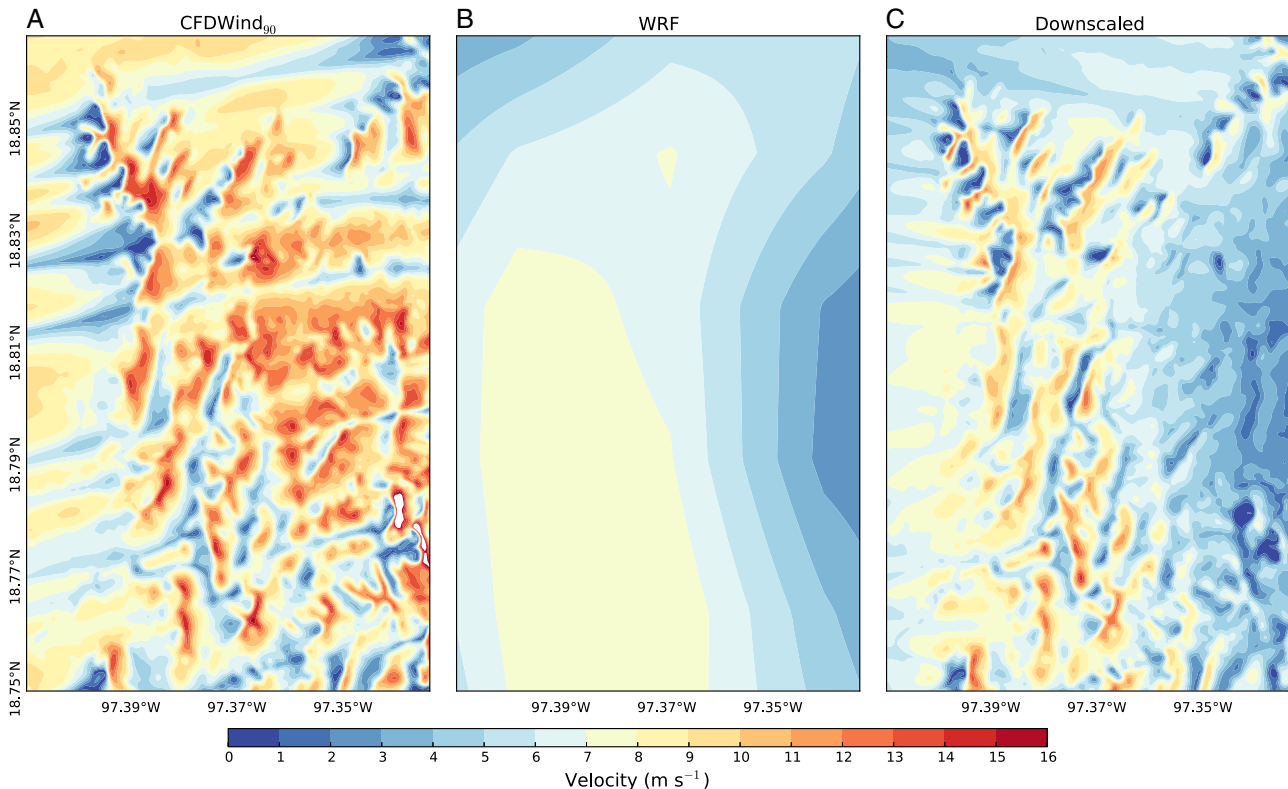Note: WRF model is used as reference model in the SS% calculations.

FIGURE 7 Wind velocity at 10-m height on July 3, 2013 at 6 am (LT). A, Precomputed Alya-CFDWind solution u_{CfD}^{90} (ie, assuming a 90° geostrophic wind direction); B, WRF at 3-km resolution; and C, resulting downscaled field assuming a value of $\Re = 500$ m for the transfer functions [Colour figure can be viewed at wileyonlinelibrary.com]
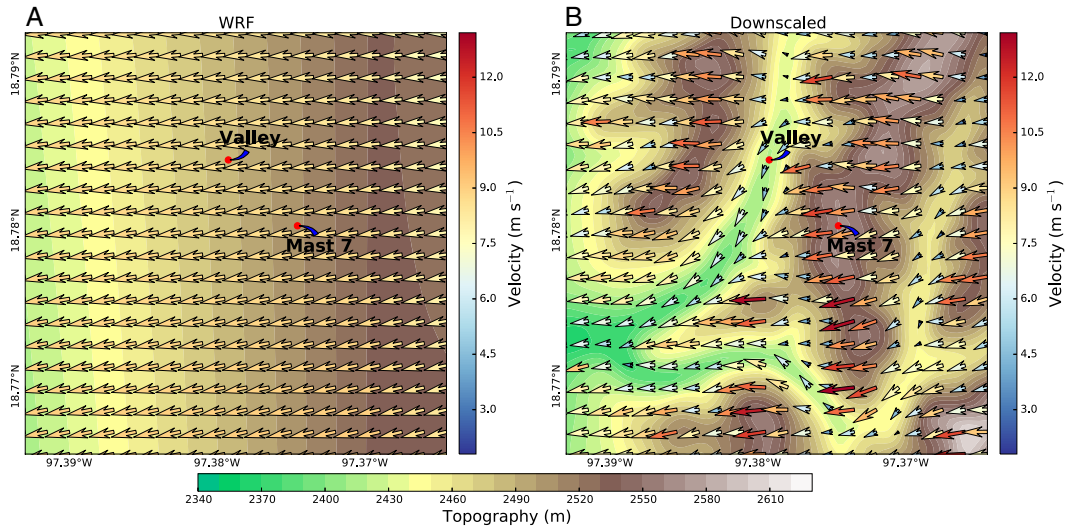
FIGURE 8 A, WRF wind velocity vectors at 10-m height on July 3, 2013 at 6 am (LT). B, Wind field after downscaling using a radius of influence of $\Re_{500}$. Plots cover an area of 3×3 km^2 that corresponds to one WRF cell and include Mast-7 (red dot) and a small valley 500 m west (not visible at mesoscale resolution) [Colour figure can be viewed at wileyonlinelibrary.com]
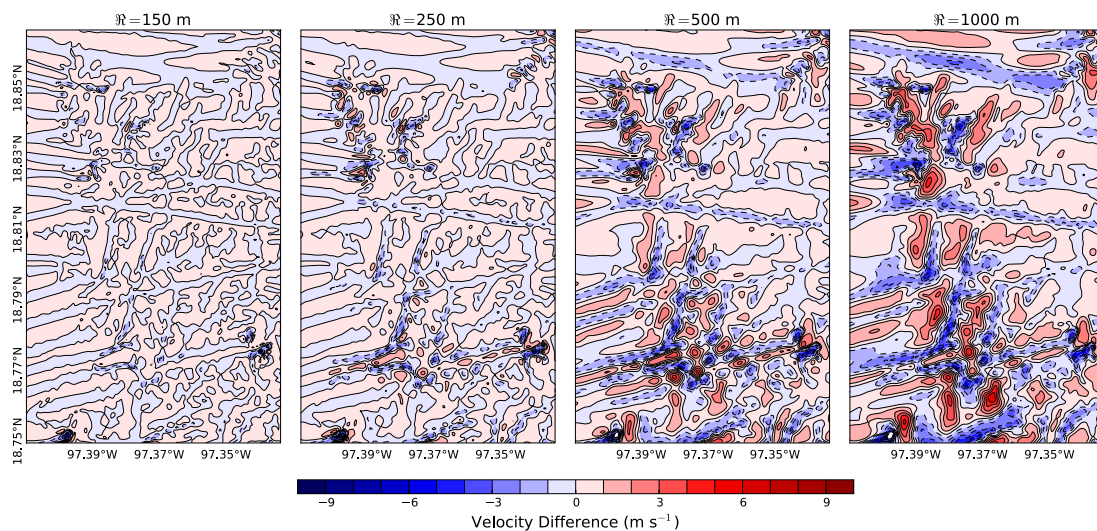

FIGURE 9 Wind velocity differences between the downscaled and the WRF fields considering a radius of influence of 150, 250, 500, and 1000 m from left to right. Results at height 80 m above the terrain for July 3, 2013 at 6 am (LT) [Colour figure can be viewed at wileyonlinelibrary.com]

velocity field coincides with that of WRF. In this particular example, $\Re_{150}$ differences are less than 1 m s^{-1} for all points of the domain. In contrast, as $\Re$ increases, the transfer functions incorporate more local wind velocity fluctuations around the mean mesoscale component and, in consequence, more local terrain effects appear in the downscaled field. Figure 10 shows the July 3, 2013, time series of results at Mast-7 site (80-m height). During this particular day, the mesoscale forecast did not capture well the observed wind variability. Comparing WRF and different $\Re$ cases, the downscaled results follow the mesoscale pattern adding a correction factor that depends on the terrain and on the value of $\Re$ used. In this location (Mast-7), the different $\Re$ cases result on a wind velocity increase and little direction variations, with a maximum wind veering of about 5°. In contrast, Figure 11 shows the same time series of results but at the valley (valley point in Figure 8), where no observations are available. At this location, the downscaling corrections are much more pronounced, with the transfer functions decreasing the mesoscale velocity by 10% to 35% (depending on $\Re$) and a wind veering correction of about 8° along the period (at 80-m height above terrain).

In summary, the downscaled fields contain the mesoscale pattern; the smaller the value of $\Re$, the more the downscaled velocity field tends to that of WRF; the corrections introduced by the downscaling methodology increase as one approaches the ground surface and; valleys and channelling zones show larger differences than elevated locations.
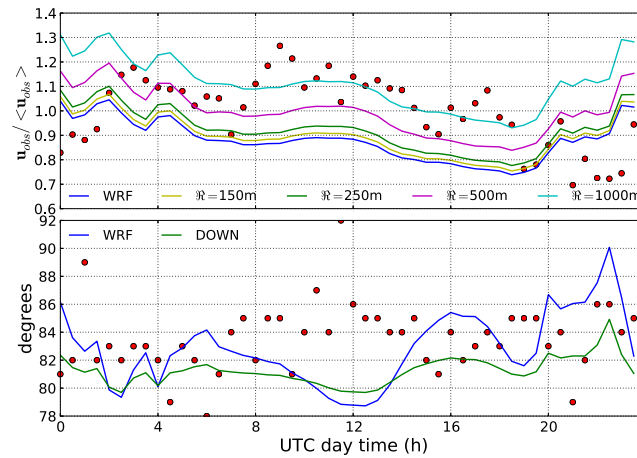
FIGURE 10 Time series of wind velocity and direction at Mast-7 during July 3, 2013. Results at 80 m height. Wind velocity is normalised to the day-mean of observations. Red dots represent observations (averaged over 30 minutes), blue lines show the WRF forecast, and the rest of lines show the downscaled values for different radii of influence, from 150 to 1000 m [Colour figure can be viewed at wileyonlinelibrary.com]
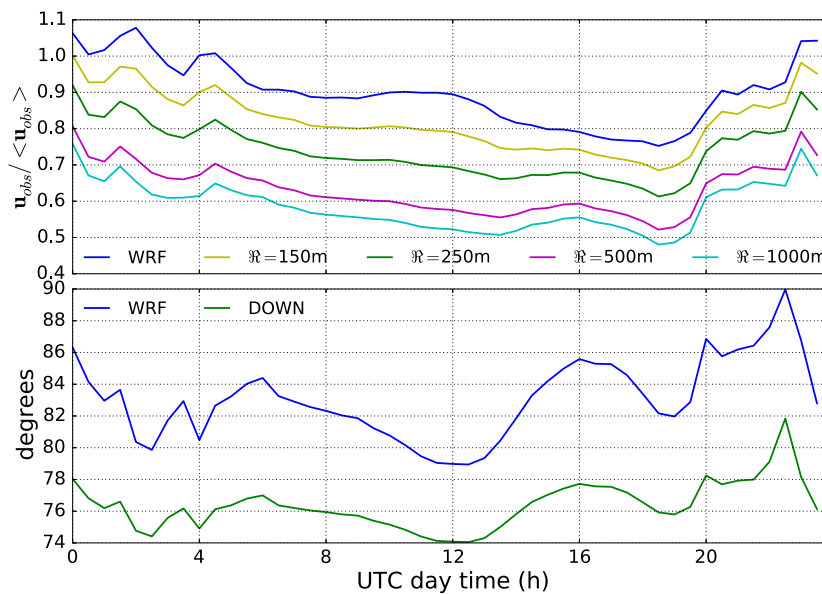

FIGURE 11 Same in Figure 10 but at the valley point, where no observations exist [Colour figure can be viewed at wileyonlinelibrary.com]

5.2 | Quantitative validation

A couple of comments are necessary before performing the quantitative validation of the downscaling methodology for the 9-month period. First of all, substantial differences between mesoscale WRF forecasts and 10-minute averaged mast observations can occur due to a number of reasons. Causes of erroneous forecasting intervals may include WRF model asynchrony (eg, delay/advance on the predicted arrival time of a front, the starting point of a convective event, and thermal winds), loose of the mesoscale pattern by the model, or wind direction meandering during periods of low wind intensity. Regardless of its origin, model errors generated in the mesoscale range are dragged down to the microscale and could offer a blurred vision of the downscaling methodology. For this reason, we filtered out from the dataset all the velocity-direction pairs in which the WRF direction errors at masts were larger than 60° and/or the observed velocities were less than 4 m s^{-1}. On the other hand, it has already been pointed out that masts were deployed (for wind resource assessment purposes) at locations where the synoptic and mesoscale component dominate. As a result, small differences between the mesoscale and downscaled fields are expected at the sites used for validation.

Tables 6 and 7 show the validation results for the 9-month period, classifying the results depending on observation height. Note that Table 7 does not differentiate $\mathfrak{R}$ cases because the transfer functions only apply to the velocity modulus. Looking at Table 6, ME values show a similar pattern for all heights, ie, as $\mathfrak{R}$ increases the downscaling tends to overestimate the wind velocity. In addition, the RMSE and the SS% show a worsening of the downscaled wind velocity as $\mathfrak{R}$ increases. The worst value of SS% (more negative) is obtained for $\mathfrak{R}_{1000}$, whereas the $\mathfrak{R}_{150}$ and the $\mathfrak{R}_{250}$ cases

TABLE 6 Mean Error (ME), Root Mean Square Error (RMSE) (in m s^{-1}), and Skill Score (SS%) for wind velocity at 11 masts during the 9-month validation period depending on the data acquisition heights (40, 60, and 80 m)

	40 m			60 m			80 m		
	ME	RMSE	SS%	ME	RMSE	SS%	ME	RMSE	SS%
$\Re_{150}$	−0.5	3.3	−0.7	−0.2	3.1	−0.8	−0.2	3.3	−0.8
$\Re_{250}$	−0.2	3.3	−2.2	0.0	3.2	−2.6	0.0	3.3	−2.7
$\Re_{500}$	1.1	3.8	−32.0	0.8	3.4	−19.7	0.7	3.6	−18.3
$\Re_{1000}$	2.6	4.8	−116.6	1.9	4.1	−75.2	1.7	4.2	−58, 3

Note: Downscaling results with different radii of influence $\Re$ for the transfer functions are shown. WRF model is used as reference model in the SS% calculations.

TABLE 7 Downscaling Root Mean Square Error (RMSE) and Skill Score (SS%) for wind direction (in °) at 11 masts during the 9-month validation period depending on the data acquisition heights (40, 60, and 80 m)

40 m		60 m		80 m	
RMSE	SS%	RMSE	SS%	RMSE	SS%
15.5	11.0	16.5	6.9	16.9	6.8

Note: WRF model is used as reference model in the SS% calculations.

TABLE 8 Downscaling Mean Error (ME), Root Mean Square Error (RMSE), and Skill Score (SS%) for wind velocity (m s^{-1}) and direction (°)during the 9-month period

		Velocity		Direction	
Velocity bin	ME	RMSE	SS%	RMSE	SS%
4 < vel < 8	1.3	3.3	−11.1	19.5	5.2
8 < vel < 12	−0.4	3.0	−2.6	14.6	9.6
vel > 12	−2.6	3.8	10.6	11.2	19.7
Velocity bin	ME	RMSE	SS%	RMSE	SS%
Stable	−2.9	4.1	4.7	18.7	7.4
Neutral	−0.3	2.7	2.3	15.3	10.0
Unstable	1.0	3.2	−8.6	15.8	7.6

Note: Results are classified in wind velocity and atmospheric stability bins. WRF model is used as reference model in the SS% calculations.

show similar performance than WRF. Contrasting to these results, Table 7 shows that the downscaled wind direction slightly improves with respect to WRF (positive SS%).

Table 8 disaggregates the $\Re_{250}$ case for the 9-month validation period distinguishing three different stability classes (Section 4.6) and 3 different velocity bins of 4 m s^{-1} ≤ $\mathbf{u}_{obs}$ < 8 m s^{-1}, 8 m s^{-1} ≤ $\mathbf{u}_{obs}$ < 12 m s^{-1}, and $\mathbf{u}_{obs}$ ≥ 12 m s^{-1}. As observed, the downscaling skill scores improve as the velocity increases and outperforms those of WRF at high velocities. The downscaling also improves WRF results (positive SS%) in near-neutral and stable stability regimes, where buoyancy forces and vertical convective effects are supposed residual. These results are directly related to the fact that the precomputed Alya-CFDWind fields have been obtained assuming neutral stability. Regarding wind direction, Table 8 also shows that the downscaling results outperform those of WRF for all velocity bins and stability classes. To complement these results, Figure 12 shows the velocity error difference for all pairs forecast observation in the 9-month validation period depending on stability and wind velocity (using pairs of data with observed velocities greater than 8 m s^{-1}). Red dots in this figure mean that the downscaling improves the WRF forecast, whereas blue dots indicate the opposite. As observed, error differences at the measuring sites (11 masts) range between -1.2 and 1.2 m s^{-1}. The plot clearly reveals 2 well-defined regions, a blue-dominated zone (WRF is better than the downscaled field) and a red-dominated zone (downscaled field is better than WRF). Blue-dominated zone expands over the region with lower velocities and within the unstable regime, where buoyancy forces dominate. Conversely, the red-dominated zone covers the region with higher velocities and within near-neutral and stable regimes.
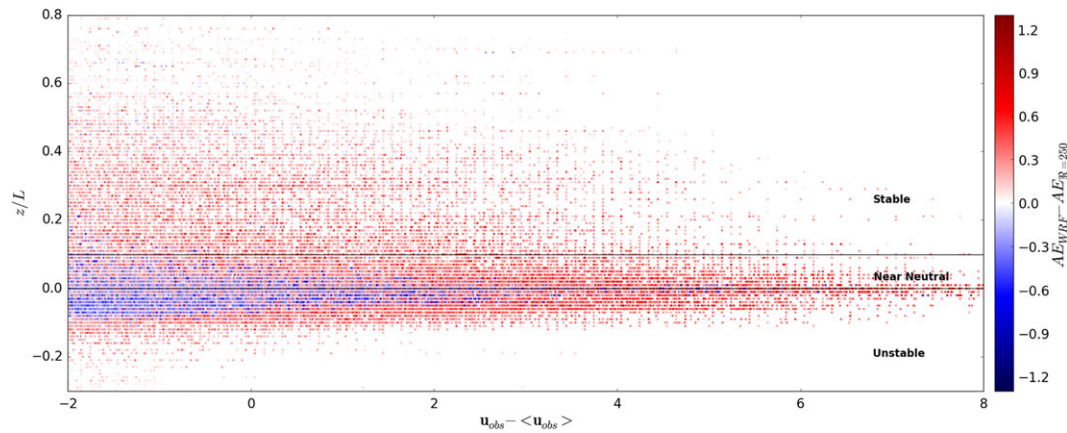
FIGURE 12 Scattered differences of absolute error $AE_{WRF} - AE_{\mathfrak{R}=250}$ (in m s^{-1}) for all pairs forecast-observation in the 9-month period where the observed velocities exceeded 8 m s^{-1}. Positive values (red points) indicate the downscaling results improve WRF whereas negative values (blue points) indicate the opposite. Results depending on the stability class (z/L) and observed wind velocity (expressed as the difference with respect to the mean value of observations $\mathbf{u}_{obs} - <\mathbf{u}_{obs}>$ in m s^{-1}) [Colour figure can be viewed at wileyonlinelibrary.com]

6 | SUMMARY AND DISCUSSION

A novel mesoscale-to-microscale downscaling methodology to forecast near-surface high-resolution winds has been presented. The methodology combines a domain segmentation technique to preserve the mesoscale pattern with the use of transfer functions to incorporate the unresolved mesoscale model subgrid terrain forcing effects (topographic effects). The downscaled near-surface wind field is obtained at 2D terrain following planes by merging segment-wise solutions obtained from precomputed Alya-CFDWind reference simulations. Because of the blending process, a certain mass unbalance may occur even if each segment solution verifies the continuity equation. However, we have estimated that this unbalance resulting from blending is, at most, of the order of $\nabla \cdot \mathbf{u}_{down} < 10^{-3}$ s^{-1} at all points.

The downscaling methodology has been validated against experimental data from a network of masts deployed at elevated zones within a complex terrain site at Puebla, Mexico. Unfortunately, the dataset did not allow us to quantify the gain at points where more pronounced microscale effects can be expected (eg, valleys and channelling zones). Downscaled near-surface wind fields incorporate terrain forcing speed-up effects at the top of the ridges while, in contrast, winds slow down and rotate at valleys and channelling zones. For the 9-month validation period, the downscaling methodology slightly improved the WRF model forecasts at masts in stable and near-neutral atmospheric regimes and for high wind velocities. In contrast, downscaling results did not show improvement during unstable regimes and during low wind velocities, where thermal effects prevail. This can be explained by the assumption of neutral stability in the precomputed Alya-CFDWind fields and evidences the need to incorporate the diurnal cycle thermal effects into the Alya-CFDWind simulations in a future.

In terms of operational wind forecasting, a major advantage of the methodology is that it incorporates physical aspects of CFD models (not captured by simpler mass-consistent models) without adding substantial computational cost. For example, running the downscaling for a 48-hour forecast window (30-min outputs) considering 5 planes of 13×8 km^2 at 40-m resolution with $\mathfrak{R} = 250$ m takes only around 3 minutes on a standard laptop PC. The computing time depends on the value of $\mathfrak{R}$ (larger values of $\mathfrak{R}$ require more computing time because of the spatial average), but in any case, this supposes a small percentage of the mesoscale model forecast computing time. Furthermore, these downscaling computing times could be drastically reduced by parallelising the downscaling code.

The downscaling methodology is though to be applied to any mesoscale-microscale combination of models. The current approach has considered the Coriolis term and the mixing length limitation in Alya-CFDWind simulations. Authors have considered this approach appropriate because Coriolis force affects the wind profile introducing a rotation with height, and a non-logarithmic wind profile above the surface layer (of around 100 metres). The masts at Puebla site are located at different heights and Coriolis force affects the relative wind direction and speed between them. In addition, the surface layer approximation is valid up to 100-m height, but the Puebla site has topographic height differences of about 1000 m. However, the mixing length limitation applied assumes values from homogeneous flat terrain. This is a well-known open problem in atmospheric RANS models, and to authors knowledge, no expression exists for the maximum mixing length on complex terrains. Thus, further research is needed to solve this issue.

In future developments, we plan to include atmospheric stability in the microscale Alya-CFDWind precomputed runs, ie, to consider a diurnal cycle for each geostrophic reference direction rather than a steady-state neutral solution. We also plan to develop and adaptive radius of influence $\mathfrak{R}(x, y, z)$ that could take into account terrain information. On the other hand, the methodology will be implemented in the operational model chain of the regional meteorological service of Catalonia for an extensive validation and possible exploitation.

ORCID

Jordi Barcons http://orcid.org/0000-0001-5550-1986

REFERENCES

1. Orlanski I. A rational subdivision of scales for atmospheric processes. *Bull Am Met Soc.* 1975;56:527-530.

2. Kitada T, Kaki A, Ueda H, Peters LK. Estimation of vertical air motion from limited horizontal wind data numerical experiment. *Atmos Environ (1967)*. 1983;17(11):2181-2192.

3. Homicz G. Three-dimensional wind field modeling: a review. Technical Report August, Sandia National Laboratories, Albuquerque, SANDIA; 2002. http://prod.sandia.gov/techlib/access-control.cgi/2002/022597.pdf.

4. Wagenbrenner NS, Forthofer JM, Lamb BK, Shannon KS, Butler BW. Downscaling surface wind predictions from numerical weather prediction models in complex terrain with WindNinja. *Atmos Chem Phys.* 2016;16(8):5229-5241.

5. Ehrhard J, Khatib I, Winkler C, Kunz R, Moussiopoulos N, Ernst G. The microscale model MIMO: development and assessment. *J Wind Eng Ind Aerodyn.* 2000;85(2):163-176.

6. Arroyo RC, Rodrigo JS, Gankarski P. Modelling of atmospheric boundary-layer flow in complex terrain with different forest parameterizations. *J Phys: Conf Ser.* 2014;524:1-13.

7. Castro FA, Silva Santo C, Lopes da Cost JC. One-way mesoscale-microscale coupling for the simulation of atmospheric flows over complex terrain. *Wind Energy*. 2015;18:1251-1272.

8. Udina M, Sun J, Kosović B, Soler MR. Exploring vertical turbulence structure in neutrally and stably stratified flows using the weather research and forecasting large-eddy simulation (WRF-LES) Model. *Boundary-Layer Meteorol.* 2016;161(2):355-374.

9. Zajaczkowski FJ, Haupt SE, Schmehl KJ. A preliminary study of assimilating numerical weather prediction data into computational fluid dynamics models for wind prediction. *J Wind Eng Ind Aerodyn.* 2011;99(4):320-329.

10. Sanz Rodrigo J, Churchfield M, Kosović B. A wind energy benchmark for abl modelling of a diurnal cycle with a nocturnal low-level jet: Gabls3 revisited. *J Phys: Conf Ser.* 2016;753:1-12.

11. Sanz Rodrigo J, Garcia B, Cabezón D, Lozano S, Martí I, García B. Downscaling mesoscale simulations with CFD for high resolution regional wind mapping. In: Proc. European Wind Energy Conference; 2010; Warsaw, Poland. 1-8.

12. Skamarock WC, Klemp JB, Dudhia J, et al. A description of the Advanced Research WRF Version 3. Technical Report NCAR/TN-475+STR, National Center for Atmospheric Research. Boulder, Colorado, USA: 2008.

13. Hong SY, Lim JOJ. The WRF single-moment 6-class microphysics scheme (WSM6). *J Korean Meteor Soc.* 2006;42(2):129-151.

14. Kain JS. The Kain-Fritsch convective parameterization: an update. *J Appl Meteor*. 2004;43:170-181.

15. Janjic ZI. The surface layer in the NCEP Eta Model. In: Eleventh Conference on Numerical Weather Prediction, Norfolk, VA, 19-23 August; Amer. Meteor. Soc.; 1996; Boston, MA:354-355.

16. Chen F, Dudhia J. Coupling an advanced land surface–hydrology model with the penn state–NCAR MM5 modeling system. Part I: Model implementation and sensitivity. *Mon Wea Rev*. 2001;129:569-585.

17. Janjic Z. The step-mountain eta coordinate model: further developments of the convection, viscous sublayer and turbulence closure schemes. *Mon Wea Rev*. 1994;122:927-945.

18. Mlawer EJ, Taubman SJ, Brown PD, Iacono MJ, Clough SA. Radiative transfer for inhomogeneous atmospheres: RRTM, a validated correlated-k model for the longwave. *J Geophys Res*. 1997;102:16663-16682.

19. Dudhia J. Numerical study of convection observed during the winter monsoon experiment using a Mesoscale two-dimensional model. *J Atmos Sci*. 1989;46(20):3077-3107.

20. Avila M, Folch A, Houzeaux G, Eguzkitza B, Prieto L, Cabezon D. A parallel CFD model for wind farms. *Procedia Comput Sci*. 2013;18:2157-2166.

21. Apsley D, Castro I. A limited-length-scale k-ε model for the neutral and stably-stratified atmospheric boundary layer. *Boundary-Layer Meteorol*. 1997;83(1):75-98.

22. Houzeaux G, Vázquez M, Aubry R, Cela JM. A massively parallel fractional step solver for incompressible flows. *J Comput Phys*. 2009;228(17):6316-6332.

23. Vázquez M, Houzeaux G, Koric S, et al. Alya: multiphysics engineering simulation toward exascale. *J Comput Sci*. 2016;14:15-27.

24. Gargallo-Peiró A, Avila M, Owen H, Prieto L, Folch A. Mesh generation for atmospheric boundary layer simulation in wind farm design and management. *Procedia Eng*. 2015;124:239-251.

25. Blackadar AK. The vertical distribution of wind and turbulent exchange in a neutral atmosphere. *J Geophys Res*. 1962;67:3095-3102.

26. Monin AS, Obukhov A. Basic laws of turbulent mixing in the surface layer of the atmosphere. *Contrib Geophys Inst Acad Sci USSR*. 1954;151:163-187.

27. Persson A. User guide to ECMWF forecast products. Technical Report, ECMWF; 2015.